AGU PUBLICATIONS

JGR

Journal of Geophysical Research: Oceans

RESEARCH ARTICLE

10.1002/2015JC011523

On the stability and spatiotemporal variance distribution of salinity in the upper ocean

Terence J. O'Kane[1], Didier P. Monselesan[1], and Christophe Maes[2]

[1]CSIRO Oceans and Atmosphere, Hobart, Tasmania, Australia, [2]Université Brest, Ifremer, CNRS, IRD, Laboratoire d'Océanographie Physique et Spatiale (LOPS), IUEM, Brest, France

Key Points:
- Salinity variations due to changes in the static stability, intrinsic ocean, or internal climate
- Partition salinity variance in time via singular spectral analysis
- In the subtropics, salinity largely acts to destabilize the upper ocean stratification

Supporting Information:
- Supporting Information S1
- Movie S1

Correspondence to:
T. J. O'Kane,
terence.okane@csiro.au

Citation:
O'Kane, T. J., D. P. Monselesan, and C. Maes (2016), On the stability and spatiotemporal variance distribution of salinity in the upper ocean, *J. Geophys. Res. Oceans*, *121*, 4128–4148, doi:10.1002/2015JC011523.

Received 2 DEC 2015
Accepted 5 MAY 2016
Accepted article online 13 MAY 2016
Published online 18 JUN 2016

Abstract Despite recent advances in ocean observing arrays and satellite sensors, there remains great uncertainty in the large-scale spatial variations of upper ocean salinity on the interannual to decadal timescales. Consonant with both broad-scale surface warming and the amplification of the global hydrological cycle, observed global multidecadal salinity changes typically have focussed on the linear response to anthropogenic forcing but not on salinity variations due to changes in the static stability and or variability due to the intrinsic ocean or internal climate processes. Here, we examine the static stability and spatiotemporal variability of upper ocean salinity across a hierarchy of models and reanalyses. In particular, we partition the variance into time bands via application of singular spectral analysis, considering sea surface salinity (SSS), the Brunt Väisälä frequency (N2), and the ocean salinity stratification in terms of the stabilizing effect due to the haline part of N2 over the upper 500m. We identify regions of significant coherent SSS variability, either intrinsic to the ocean or in response to the interannually varying atmosphere. Based on consistency across models (CMIP5 and forced experiments) and reanalyses, we identify the stabilizing role of salinity in the tropics—typically associated with heavy precipitation and barrier layer formation, and the role of salinity in destabilizing upper ocean stratification in the subtropical regions where large-scale density compensation typically occurs.

1. Introduction

In a recent study, *Monselesan et al.* [2015] examined the spatiotemporal patterns of sea level anomalies (SLA) and sea surface temperatures (SST), prognostic variables each reflecting different elements of the dynamically important regions of the oceans in terms of large variance in the climate system. At first-order, SLA provides a depth integrated measure of sea water density anomalies, combining temperature (thermosteric component, approximately proportional to heat content) and salinity (halosteric component) changes. The temporal characteristics of SLA variance should provide a good indication of the most dynamically active regions of the ocean where significant mixing of heat into the layer above the thermocline occurs. Anomalous SST (SSTA) is a surface measure indicating changes in near surface ocean heat and the coupling to the atmosphere and, while less indicative of the dynamics of the upper ocean, provides a good indication of regions where ocean-atmosphere heat fluxes are anomalously large. Sea surface salinity (SSS) on the other hand is an indicator of key atmosphere-ocean processes associated with the hydrological cycle [*Yu*, 2012; *Reul et al.*, 2014]. Beyond seasonal variations, decadal salinity variability reflects also differences in evaporation and precipitation fluxes at the surface, whereas in the subsurface it contributes to steric sea level change and freshwater/salt transports [*Vargas-Hernandez et al.*, 2015].

Estimates of the global distribution of SSS have been dramatically transformed over the recent decade by the deployment of the Argo profiling float array. While the Argo array can now provide monthly SSS estimates at a horizontal grid resolution of a few hundred square kilometers, there is at present insufficient data to resolve interannual to decadal SSS variability, although this situation will be improved as satellite data becomes increasingly available from the SMOS [*Kerr et al.*, 2010; *Font et al.*, 2013; *Maes et al.*, 2014] and Aquarius/SAC-D [*Lagerloef et al.*, 2008; *Lagerloef*, 2012] missions.

Consistent with simple thermodynamic arguments, i.e., Clausius-Claperyon, and climate model projections, observational reconstructions of multidecadal trends in both global [*Antonov et al.*, 2002; *Boyer et al.*, 2005; *Hosoda et al.*, 2009; *Roemmich and Gilson*, 2009; *Durack and Wijffels*, 2010; *Durack et al.*, 2012] and regional

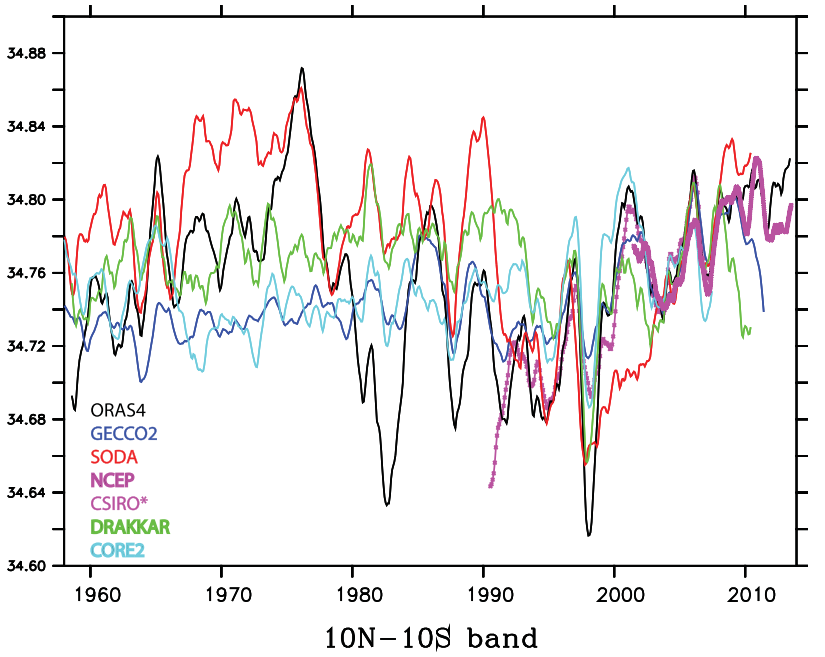

Figure 1. Time series of SSS values (psu) averaged between (180°E–180°W, 10°S–10°N) including reanalyses: ORAS4 (black), GECCO2 (blue), SODA (red), NCEP (thick purple), and CSIRO (thin purple with stars); forced ocean models: DRAKKAR (green), CORE2 (light blue). The NCEP ocean reanalysis uses only in situ data (D. Behringer, personal communication, 2014). An offset has been applied to all time series and referenced to the NCEP series, with values of 0.15 (ORAS4), 0.12 (DRAKKAR), 0.05 (SODA), −0.1 (GECCO2), 0.1 (CORE2), and 0.1 (CSIRO), respectively. A 13 month Hanning filter has also been applied to all time series.

[*Curry et al*., 2003; *Grodsky et al*., 2006; *Delcroix et al*., 2007; *Cravatte et al*., 2009] salinity point to an intensification of the hydrological cycle. One caveat on such arguments is that they typically assume thermodynamic equilibrium and statistical stationarity of the underlying data and that the observed linear trends arise largely as a result of the influence of external covariates, for example increasing CO2 contributing to anthropogenic warming.

Due to the paucity of global observations, recent estimates of long-term SSS changes (linear trends) [*Durack and Wijffels*, 2010; *Durack et al*., 2012] are necessarily biased toward the most recent decades post 1990, and in particular to the Argo period post 2001. In addition, estimates of SSS variability based on ocean models and reanalyses show a certain degree of spread. To illustrate this point, we consider a simple calculation of tropical SSS averaged between 10°S and 10°N (Figure 1), comparing a range of state-of-the-art reanalyses and forced ocean models thereby demonstrating the huge uncertainties in reliably estimating the long-term variability of SSS prior to the deployment of Argo profiles. Post 2001 however, there is a dramatic reduction in the spread across the reanalyses as data from Argo profiles becomes available and the models become better constrained.

Given the lack of observational data and large uncertainties in reanalyses over the period prior to Argo, we propose a hierarchical approach to understand the variability of upper ocean salinity. Specifically, we consider intrinsic, forced, and internal salinity variability as described by long integrations from ocean general circulation model simulations and a large ensemble of CMIP5 preindustrial control simulations comprising several thousands of years of data. We then compare the spatiotemporal patterns of variability from these simulations with those from a representative 55 year ocean reanalysis and from reliable estimates from a skilful reanalysis based only on the Argo period.

The analysis here focuses on the spatiotemporal patterns of SSS and the ocean salinity stratification (OSS); here defined as the stabilizing effect (positive values) due to the haline part of the Brunt Väisälä frequency (N^2) over the upper 500 m. We also identify regions where salinity acts to destabilize the upper ocean (*OSSU*: negative values of *OSS*). We limit our focus only to those large-scale signals in salinity that are robust across models and reanalyses, and recognize that there will be many important regional signals that will not be discussed. This work builds on and extends the recent study of *Maes and O'Kane* [2014] which

Table 1. CMIP5 Models (r1i1p1-piControl Experiments)

Model	Start-End Dates (yyyymm)	Length (years)
ACCESS1-0	030001–079912	500
ACCESS1-3	025001–074912	500
bcc-csm1-1-m	000101–040012	400
bcc-csm1-1	000101–050012	500
CanESM2	201501–301012	996
CCSM4	025001–130012	1051
CESM1-BGC	010101–060012	500
CESM1-CAM5	000101–031912	318
CESM1-FASTCHEM	007001–029112	222
CESM1-WACCM	009601–029512	200
CMCC-CESM	432401–460012	277
CMCC-CM	155001–187912	330
CMCC-CMS	368401–418312	500
CNRM-CM5-2	185001–225912	400
CNRM-CM5	185001–269912	850
CSIRO-Mk3-6-0	000101–050012	500
FGOALS-g2	020101–090012	700
FIO-ESM	040101–120012	800
GFDL-CM3	000101–080012	800
GFDL-ESM2G	000101–050012	500
GFDL-ESM2M	000101–050012	500
GISS-E2-R-CC	205001–230012	251
GISS-E2-R	398101–453012	550
HadGEM2-CC	185912–209912	241
HadGEM2-ES	185912–243605	476
IPSL-CM5A-LR	180001–279912	1000
IPSL-CM5A-MR	180001–209912	300
IPSL-CM5B-LR	183001–212912	300
MPI-ESM-LR	185001–284912	1000
MPI-ESM-MR	185001–284912	1000
MPI-ESM-P	185001–300512	1156
MRI-CGCM3	185101–235012	500
NorESM1-ME	090101–115212	252
NorESM1-M	070001–120012	501

focussed only on the stabilizing effect of salinity in the upper 300 m of the tropical oceans where salinity barrier layers dominate.

In section 2, we briefly describe the model, forced model simulation experiments, and the CSIRO ocean reanalysis outputs. More detailed explanations of the model configuration, forcings, and data assimilation procedure can be found in Appendix A, B, and C, respectively. In section 3, we outline the singular spectral analysis method as applied to the model data and a formal definition of OSS. The results, discussion, and conclusions are given in sections 5 and 8.

2. Data Sets

The model used for the CORE simulations and data assimilation is the Australian Community Climate Earth System Simulator-Ocean (ACCESS-O) configuration of the GFDL MOM4p1 ocean-ice code [*Delworth et al.*, 2006], the details of which are described in Appendix A. In addition to studies of salinity barrier layers and stratification [*Maes et al.*, 2014; *Maes and O'Kane*, 2014], this configuration has been used in recent studies of multiyear to decadal variability in the Tasman Sea [*Sloyan and O'Kane*, 2015] and the Southern Ocean [*O'Kane et al.*, 2013a, 2013b, 2013c], South Pacific ocean "spiciness" and El Niño Southern Oscillation (ENSO) variability [*O'Kane et al.*, 2014] and Antarctic sea-ice variability and trends [*Matear et al.*, 2015].

Here, we are interested in ascribing various spatiotemporal patterns of the observed and modeled salinity variability at interannual to multidecadal time scales to intrinsic, internal, and forced processes. To estimate salinity variability intrinsic to the ocean, we use years 1800–1899 of a coupled ocean-sea ice spin-up with nominal year forcing (daily climatological 10 m winds with small-scale isotropic noise added), referred to as the CORE1 experiment (described in Appendix B). This data set enables the identification of those regions of the modeled ocean where coherent salinity anomalies are formed in the absence of interannual variability due to coupling to reanalyzed atmospheric winds.

To identify internal climate variability—here defined as variability associated with the internal modes of the climate system in the absence of external covariates, e.g., radiative forcing associated with anthropogenic factors—we use SSS from yearly averaged preindustrial control simulations (piControl – r1i1p1) from 34 CMIP5 models [*Taylor et al.*, 2012] listed in Table 1. To reduce the likelihood of model drift contaminating the signal, a cubic is fitted over the entire control period (typically about 500 years or longer for each model) and removed [*Sen Gupta et al.*, 2012, 2013]. The model output data are further remapped (bicubic interpolation) to a common $1^\circ \times 1^\circ$ Cartesian grid.

For the forced response of the ocean to the observed (reanalyzed) atmosphere, we again use the ACCESS-O model, but now forced with observed winds over the period 1948–2007 which we refer to as the CORE2 experiment. These experiments are described in Appendix B. We use this simulation to examine the spatiotemporal patterns of SSS variability arising directly as a response to the interannually varying atmosphere. We further use this simulation to estimate the variability of the full three-dimensional Brunt Väisälä frequency and the role salinity plays in upper ocean stratification. The simulated SSS is compared to the

ORAS4 ocean reanalysis (1950–2014) [*Balmaseda et al*., 2013], which we will regard as a plausible estimate of the observed surface salinity over the past ≈ 60 years.

The ACCESS-O model configuration, forced by CORE2 winds, forms the basis for the CSIRO reanalysis data set, where subsurface temperature, salinity (Argo, XBT, CTD), and surface satellite SST observations are jointly assimilated. Briefly described in Appendix C, this data set comprises a series of reanalyses over the period 1990–2007, although here, we focus only on the Argo period. The CSIRO reanalysis has been globally validated against in situ observations in recent studies of the multiyear to decadal variability in the Tasman Sea [*Sloyan and O'Kane*, 2015], salinity barrier layers, and stratification [*Maes et al*., 2014; *Maes and O'Kane*, 2014], South Pacific ocean "spiciness" and El Niño Southern Oscillation (ENSO) variability [*O'Kane et al*., 2014; *Maes et al*., 2014].

3. Singular Spectral Analysis

For all dedrifted preindustrial control and globally detrended reanalyzed time series, the variance in selected time-bands is computed at each grid point. Singular spectral analysis (SSA) [*Elsner and Tsonis*, 1996; *Allen et al*., 2002; *Golyandina and Zhigljavsky*, 2013] is applied to derive the in-band variance. SSA is nonparametric and data adaptive. Here we follow the approach of *Monselesan et al*. [2015]. The method decomposes a time series $x(t)$ of length L as the sum of reconstructed components derived from the covariance matrix $C(x, M)$ built on lagged versions $x(t+j-1)$ of $x(t)$ with $j=1,\ldots,M \leq (L/2)$ up to a maximum lag M called the embedding dimension. The sum of all M eigenvalues λ_k of $C(x, M)$ with $k=1,\ldots,M$ equals the total variance of $x(t)$. The original time series is recovered as the sum of reconstructed components

$$x(t)=\sum_{k=1}^{M} r_k(t), t=1,\ldots,L \tag{1}$$

with

$$r_k(t)=\frac{1}{M}\sum_{j=1}^{M} A_k(t+j-1)e_k(j) \tag{2}$$

where $A_k(t)$ are the reconstructed components

$$A_k(t)=\sum_{i=1}^{M} x(t+i-1)e_k(i) \tag{3}$$

and e_k are the eigenvectors of $C(x, M)$ such that

$$C(x,M)e_k=\lambda_k e_k, k=1,\ldots,M \tag{4}$$

The variance explained λ_M by the reconstructed components $r_M(t)$ are computed for the following embedding dimensions $M=2, 5, 10, 25, 50, 75, 100, 150, 200$ in years. In-band variances are then approximated by the variance differences $\lambda_{M_i}-\lambda_{M_{i+n}}$ at each location. The time bands considered here span 1–2, 2–5, 5–10, 10–25, 25–50, 50–75, 75–100, 100–150, and 150–200 years. The CMIP5 model ensemble in-band variance mean (Figure 3) is then constructed. The in-band fractional variance (fraction of the total) maps for SSS for each individual CMIP5 model are included in the supporting information Figures S1–S34.

In order to estimate confidence in the fractional variances in the band spanning M_i to M_{i+n} years, we have calculated the model ensemble signal-to-noise ratios *SNR*s (Figure 4), here defined as

$$SNR=\frac{\mu_{M_i}-\mu_{M_{i+n}}}{\sqrt{v_{M_i}+v_{M_{i+n}}}} \tag{5}$$

where v_{M_i} and μ_{M_i} are the model ensemble variance and average of the fractional variances explained by the low-passed signal for the embedding dimension M_i, λ_{M_i}, taken over all model preindustrial control experiments. Note that for the first band (1–2 years), the *SNR* reduces to $(1-\mu_{M_1})/v_{M_1}^{1/2}$ as there is no loss of variance for $M = 1$ (the sampling frequency; as we are using yearly averaged data and the fraction of variance explained is $\lambda_{M=1}=1$ for all models).

The SSA ensemble mean is constructed by calculating the fractional in-band variance for each model and then averaging over all models. To reiterate: *we calculate the ensemble mean of model variance and not the variance of the model ensemble mean*. That we use data from long CMIP5 preindustrial control simulations (>500 years) with climatological radiative forcings means that there is no externally forced variability and that only the internal variability of the modeled earth system is present. Of course, the reanalyzed products examined here include both internal and external sources of variability. Fractional variances are preferred because the disparate set of models can and do have quite different total variances in any given time band. By taking fractional variances relative to the total for each model (prior to averaging), we normalize each model, making the ensemble average of the individual model fractional in-band variances meaningful.

It is key to recognize that SSA works on the temporal dimension alone with the spatial maps determined by the dynamic processes in the regions of high temporal variance within a given band. This means that SSA spatial maps preferentially identify regions of coherence where dynamic modes of variability may occur. We apply SSA not only to the two-dimensional time evolving SSS but also to the Brunt Väisälä frequency (N^2) in three-dimensions plus time.

4. Ocean Salinity Stratification

We are also interested in the contribution salinity makes to N^2 or more specifically the role salinity plays in either stabilizing or destabilizing the stratification. To this end, and following *Maes and O'Kane* [2014], we approximate N^2 in terms of the vertical profiles of temperature and salinity, i.e.,

$$N^2(T,S) \approx \left(g\alpha \frac{\partial T}{\partial z} - g\beta \frac{\partial S}{\partial z} \right) \tag{6}$$

where

$$\alpha = -\rho^{-1} \frac{\partial \rho}{\partial T} \tag{7}$$

$$\beta = \rho^{-1} \frac{\partial \rho}{\partial S} \tag{8}$$

$$N_T^2(T,S) = g\alpha \frac{\partial T}{\partial z} \tag{9}$$

$$N_S^2(T,S) = N^2(T,S) - N_T^2(T,S). \tag{10}$$

Here α is the thermal expansion coefficient, β is the haline contraction coefficient, T is the temperature, S is the salinity, and z is depth. In the following, ocean salinity stratification (*OSS*) is defined as the vertical mean average of positive N_S^2 over the upper 500 m depth range, i.e., $OSS = \langle N_S^2(T,S) \rangle|_{0-500m} > 0$. N^2, *OSS* and *OSSU* are in units of s^{-2}. *Maes* [2008] showed how *OSS* allows the identification of the layer where the salinity stratification has its greatest impact on buoyancy in terms of stabilizing the water masses, typically occurring above the maximum of N^2. *OSS* measures the strength of the salinity stratification above the main thermocline and is independent of the position of the mixed layer. Where the *OSS* is negative, here denoted $OSSU = \langle N_S^2(T,S) \rangle|_{0-500m} < 0$, salinity has a destabilizing effect and can, where N^2 is attenuated, be further associated with regions of density compensation. In the results and discussion to follow, we will employ *OSS* and *OSSU* to better understand the role salinity plays in determining the ocean static stability.

5. Results

5.1. Intrinsic SSS Variability

We determine regions where SSS variability intrinsic to the ocean is likely to occur by calculating SSA fractional in band variances from the last 100 years of a long model integration forced by repeating nominal year forcing (CORE1). We observe intrinsic SSS variability in the 1–2 year time band (Figure 2) predominantly in the tropical Pacific. For the 2–5 year band, significant intrinsic SSS variability occurs in the South Indian Ocean (SIO) between 20°S and 35°S from the Western Australian coast toward Madagascar. The other region of significant intrinsic SSS variability in the 2–5 year time band occurs in the Sargasso Sea and along the Eastern

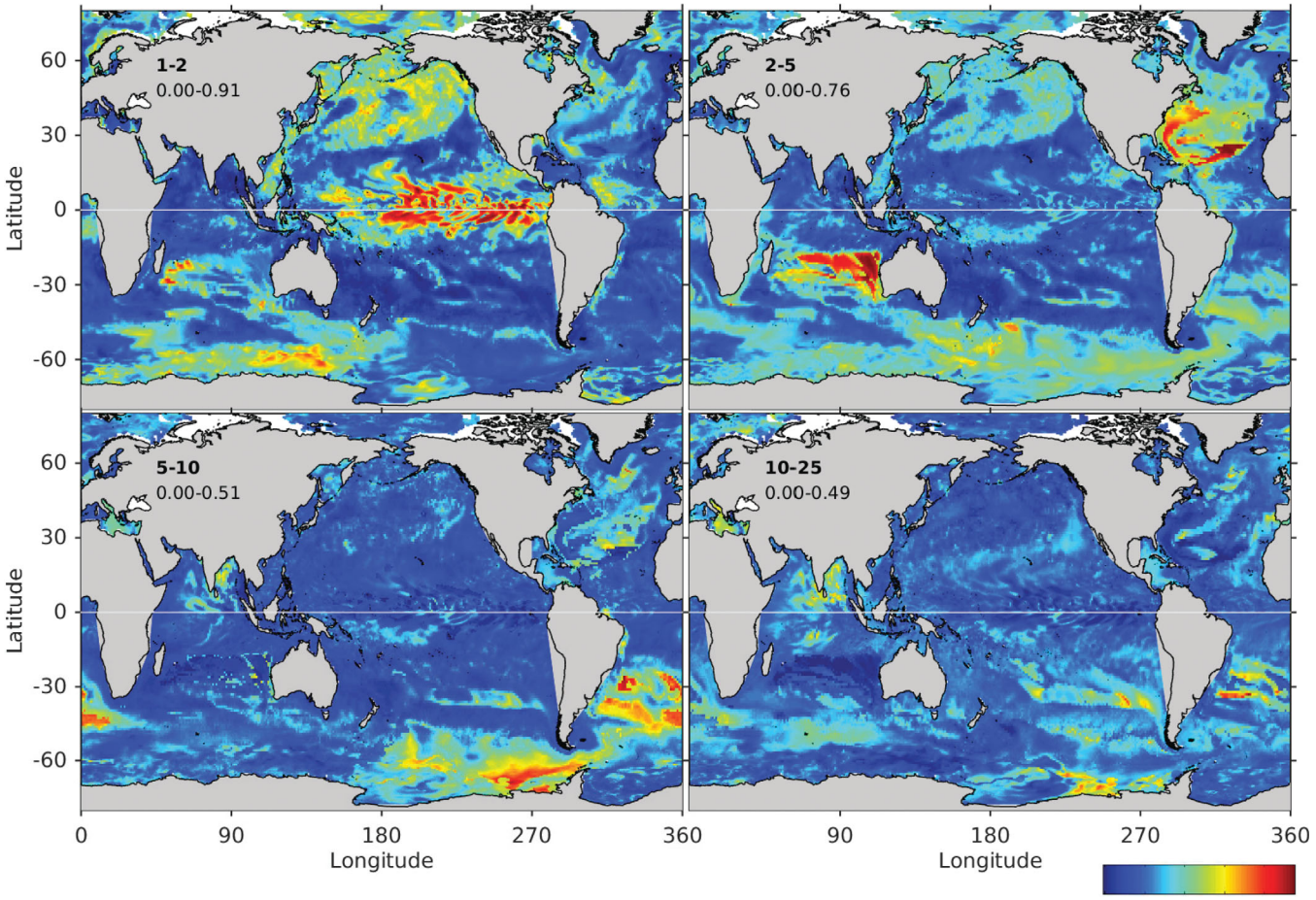

Figure 2. Fractional inband variance of intrinsic sea surface salinity (SSS) variability calculated using yearly anomalies from the climatological annual mean over years January 1800 to December 1899 of a dedrifted CORE1 (nominal year) forced ocean-sea ice simulation. Time scale bands (bold font) are in years and relative explained variance range (min-max values (normal font)) as a fraction of the total variance are given in the top left on the Eurasian continent. The shading is given by the colorbar at the bottom right with end points given by the min/max values. Shading is scaled to the variance range in each subplot such that red indicates the maximum relative explained variance and blue the minimum. The combined variance in each band sums to $1-\lambda_{M=25}$. Note that very similar patterns emerge for embeddings 2–5, 5–10, and 10–25 year time bands when monthly averages are used.

seaboard of the United States and extending into the Gulf Stream. For time bands, 5–10 and 10–25 years variance is largely localized in the subtropics from the Brazil-Malvinas confluence across to Cape Town and in the subtropical eastern South Pacific Ocean between 30°S and 40°S and in the Antarctic Circumpolar Current (ACC) about 60°S. The intrinsic variability evident in SSS extends well below the surface down to about 500 m. In supporting information, we show an animation of intrinsic salinity variability (anomalies w.r.t. the climatological mean) at 200 m depth. Here one clearly observes the origin of this variability to be coherent propagating wave trains in the North Atlantic gyre and SIO. Wave interference patterns are evident in the central Pacific. Salinity anomalies are also observed in the Bay of Bengal, the Kuroshio extension, Brazil-Malvinas confluence, and the Antarctic Circumpolar Current. This video also shows that the partition of frequency is not disconnected. Our choice of time bands (embeddings) is pragmatic but nevertheless somewhat arbitrary.

5.2. Internal SSS Variability

In order to determine the internal variability, we examine a large ensemble of CMIP5 preindustrial control simulations (Figure 3 and Table 1). We define internal variability to be the simulated large-scale climate modes of variability in the absence of any imposed external forcing signals, be that due to anthropogenic CO2, ozone mass depletion, or natural forcings such as major volcanic eruptions for example. Here anomaly SSS fractional in band variances from long simulation lengths (500 years on average) normalize the variance in each model allowing a robust signal to noise ratio (Figure 4) to be achieved when taking the ensemble average over individual model fractional in band variances (note that the fractional in band variances for

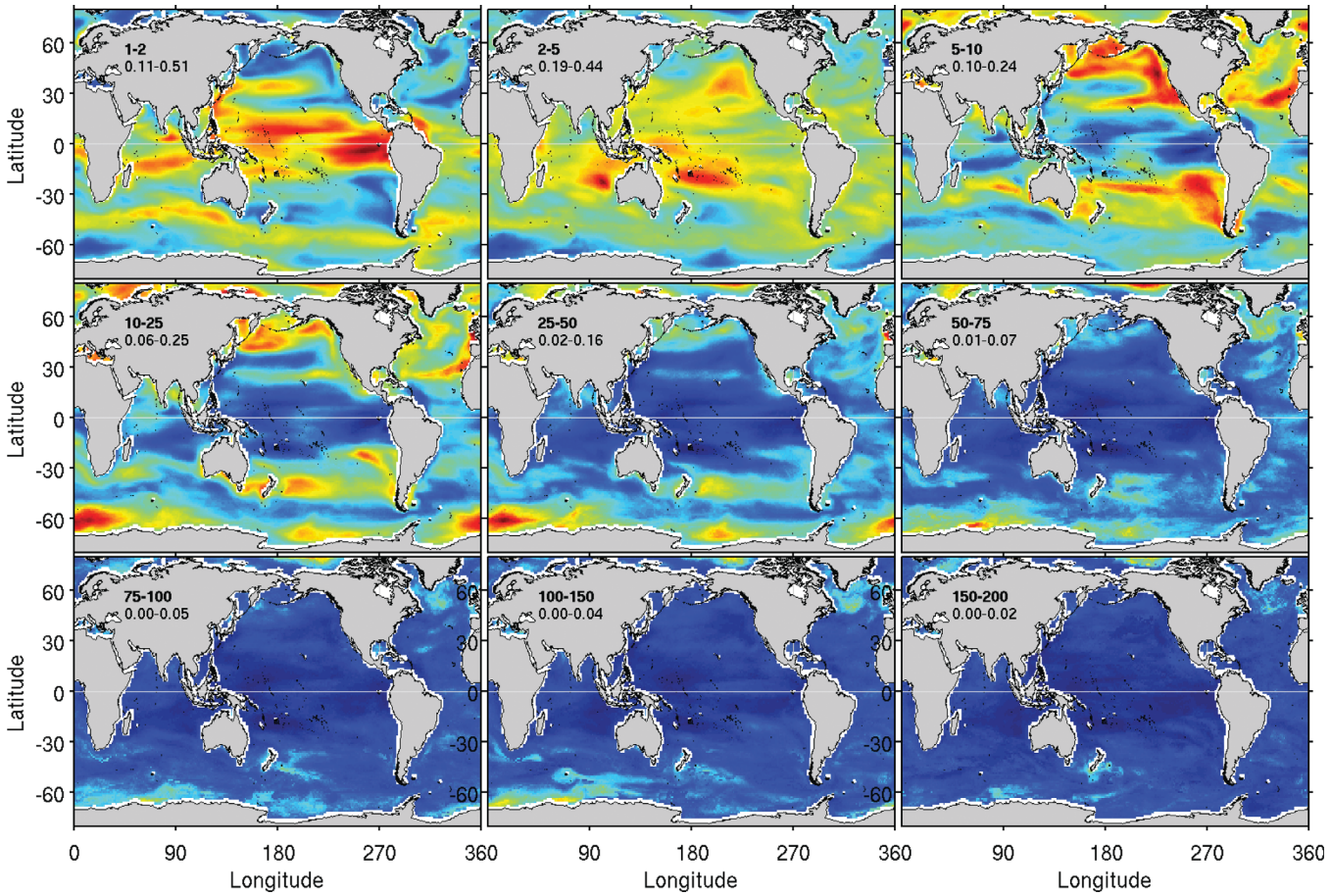

Figure 3. Ensemble mean fractional inband variance of internal SSS variability calculated using yearly anomalies from the climatological annual mean from an ensemble of dedrifted pre-industrial CMIP5 control simulations identified in Table 1. Time scale bands, relative explained variance range, and shading are as in Figure 2. The combined variance in each band sums to $1-\lambda_{M=200}$. The colorbar and shading convention is as for Figure 2.

each individual model are supplied in the supporting information). The 1–2 year internal fractional in band variances (Figure 3) occur largely in the tropics. Anomaly SSS variances in this time band are also evident in the ACC and the Kuroshio western boundary current. At 2–5 years, internal anomaly SSS variability is predominantly in the region of the South Pacific Convergence Zone (SPCZ), the tropical Eastern Indian Ocean, and to a lesser extent about Indonesian and Java.

At 5–10 years, there is a distinct shift to the subtropics and higher latitudes with little or no variance evident in the tropics between 15°S and 15°N. This pattern is also evident for the 10–25 year time band, only weaker. In the 5-10 year time band, the North Pacific as well as the subtropical South Pacific, South Indian, and North Atlantic oceans are the regions where most variance resides. As was noted for intrinsic SSS variability (Figure 2, 2–5 year band), for internal variability coherent signals emerge in the subtropical North Atlantic and eastern Indian Oceans but at the slightly longer timescales of 5–10 years with some residual signal evident in the 10–25 year band. At 10–25 years, a strong signal appears in the South African sector of Antarctica (350°E–45°E, southward of 60°S) and to a lesser extent in the region where Antarctic sea ice forms. For the 25–50 year band, the spatial pattern is little changed from the previous time band but somewhat weaker. Beyond 50 years, there is little or no surface salinity variance apart from a weak signal in the high latitudes of the North Atlantic and in the sea ice zone of the Southern Ocean.

In Figure 4, we display *SNR*s (log-scale) for the CMIP5 ensemble-averaged model simulations of anomaly SSS fractional in band variances. Here the black, grey, and light grey contours correspond to in-band variance *SNR*s equal to 6, 2, and 1, assuming no covariance across time bands. Apart from the 5–10 year time band, we see that in the tropics, the *SNR* largely exceeds 6 for embedding dimensions out to 200 years.

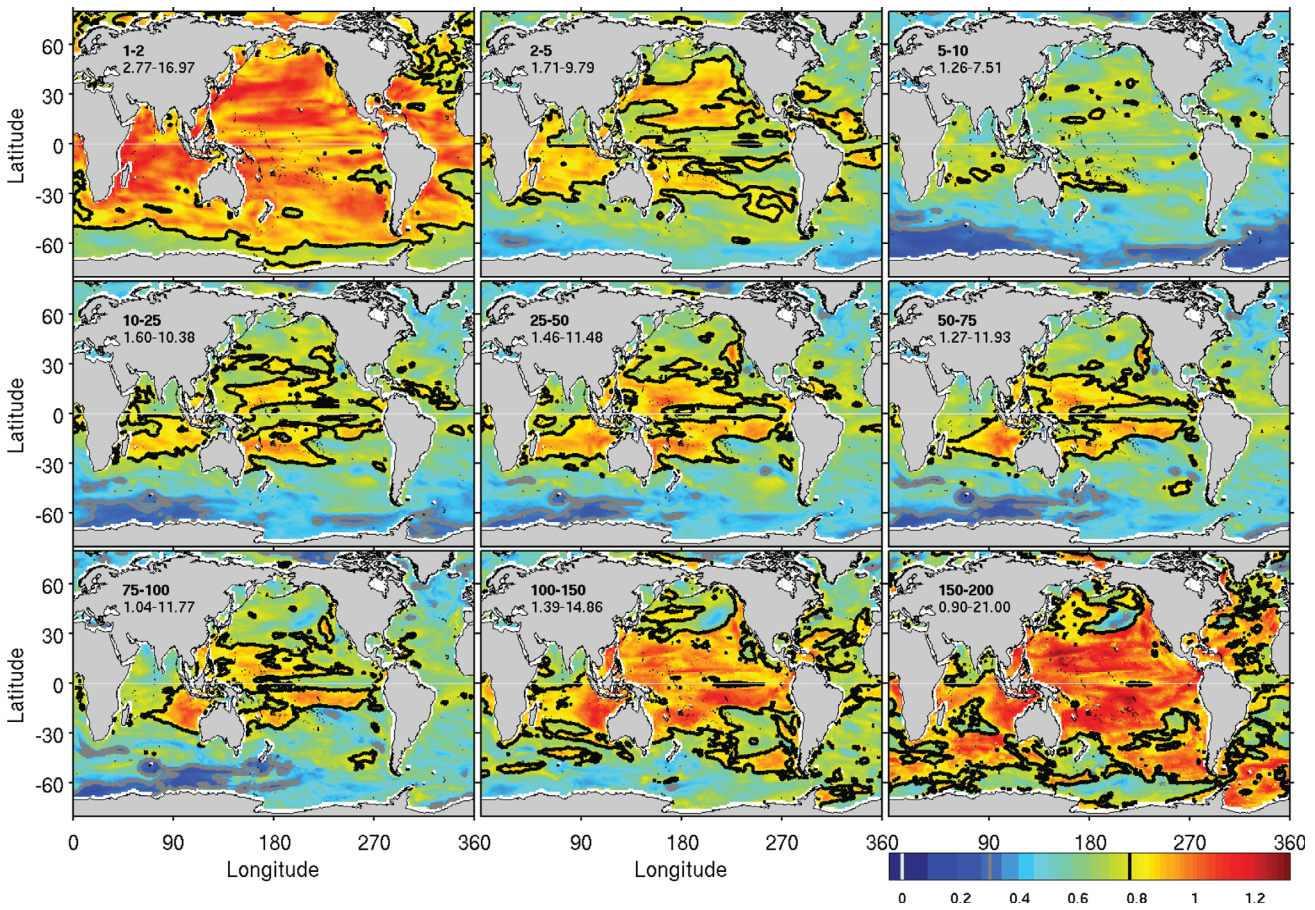

Figure 4. Calculation of the signal to noise ratio *SNR* as a measure of confidence in the CMIP5 ensemble SSS fractional in band variances shown in Figure 2 for given time bands. We display *SNR*s (log-scale) where the black, grey, and light grey contours correspond to in-band variance *SNR*s equal to 6, 2, and 1. Here we assume no covariance across time bands.

5.3. Reanalyzed Versus Modeled Anomaly SSS

To compare the observed SSS variability to a forced ocean, we use the ORAS4 reanalysis (1959–2014) and the output from our CORE2 forced (1948–2007) ocean-sea ice simulation (Figure 5). Unlike the large-scale spatially coherent patterns found in the relatively well-sampled intrinsic ocean and internal climate variances, we instead observe noisy patterns for the ORAS4 and CORE2 fractional in band variances even at the 1–2 year band. In the 2–5 year band, there is some indication of a coherent response in the SPCZ region of both reanalysis and forced model and in the 10–25 year band in the South East Pacific. We note here that the repartition in terms of amplitude between the different time bands is similar between the products, only the patterns differ, even in a large-scale perspective.

5.4. Static Stability

The importance of salinity variability is not confined at the surface only, and in order to diagnose the static stability of salinity and its part in setting the stratification, we now examine the Brunt Väisälä frequency $N^2 = -\frac{g}{\rho}\frac{\partial \rho}{\partial z}$ where g is gravity and ρ is the density. Here we take the approach of *Maes and O'Kane* [2014] applied to the 60 year CORE2 simulation and compared to the CSIRO reanalysis over the period 2001–2007. Whereas the study of *Maes and O'Kane* [2014] specifically focussed on examining daily vertical profiles of temperature and salinity, again using the CSIRO ocean reanalysis between 2001 and 2007, and the seasonal cycle of the stabilizing effect (positive values) due to the haline part of N^2 averaged over the upper 300 m, here we are interested in how the variation in the atmospheric forcing results in a differential effect in terms of the temperature and salinity stratification on interannual timescales over the upper 500 m.

We first apply the singular spectral analysis method to the calculation of the Brunt Väisälä frequency N^2 using the 60 year CORE2 simulation over the upper 500 m (Figure 6). From this calculation, we are

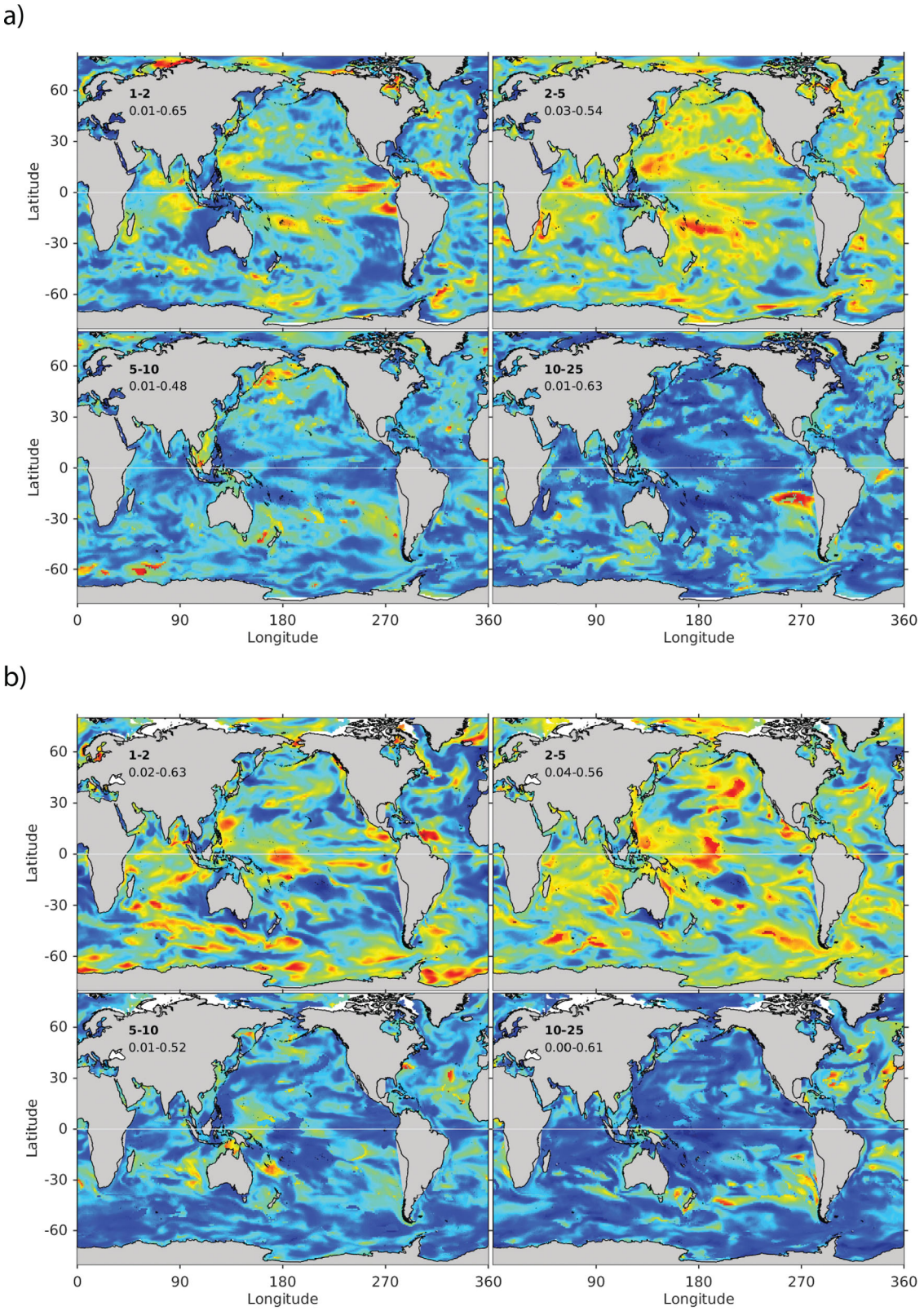

Figure 5. SSS variances calculated from the ORAS4 (January 1950 to December 2014) reanalysis and compared to those from a CORE2 (January 1948 to December 2007) forced coupled ocean-sea ice model. Again we use yearly anomalies from the climatological annual mean. Time scale bands, relative explained variance range, and shading are as in Figure 2. The combined variance in each band sums to $1-\lambda_{M=25}$. The colorbar and shading convention is as for Figure 2.

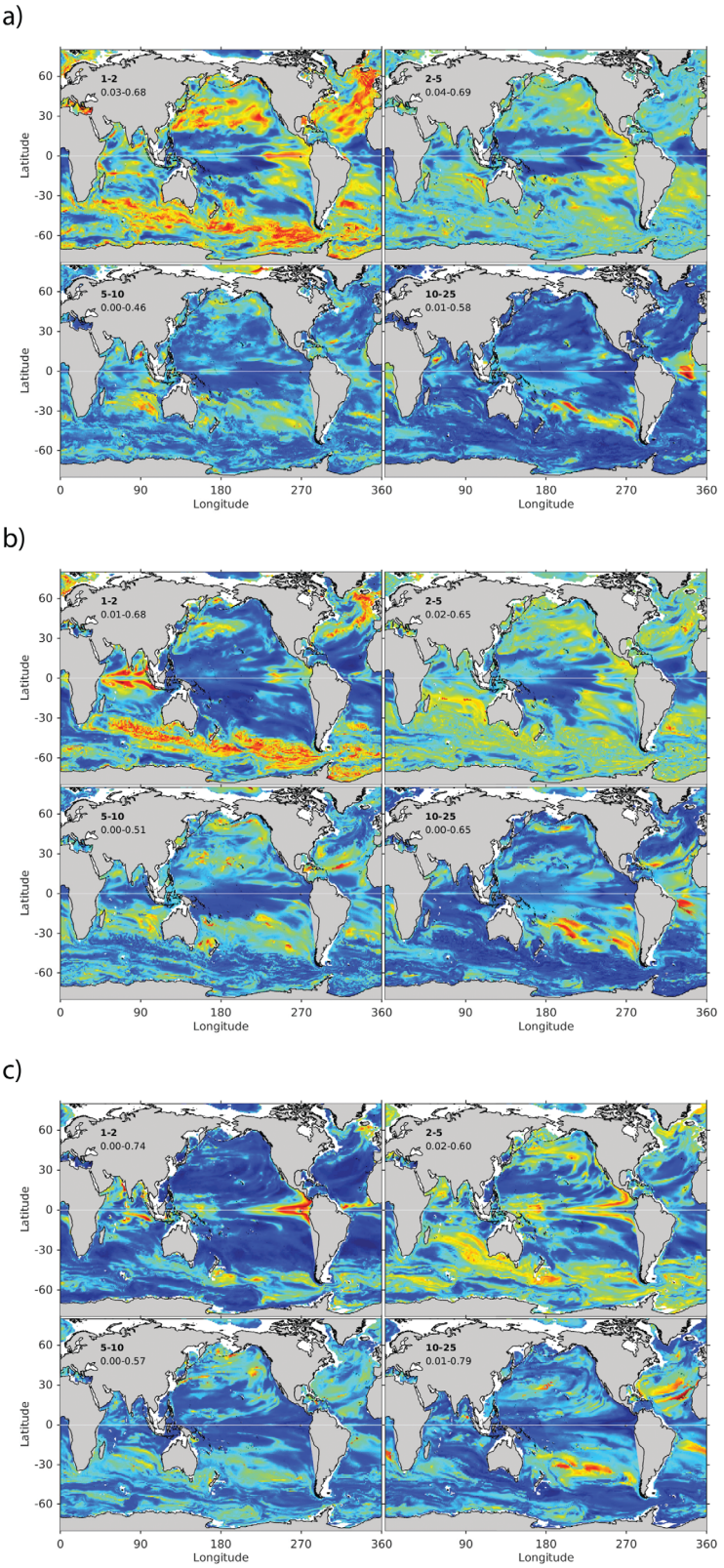

Figure 6. N^2 in units of (s^{-2}) variances at depths of 105, 205, and 427 m calculated from the CORE2 forced coupled ocean-sea ice model. Again we use yearly anomalies from the climatological annual mean. Time scale bands, relative explained variance range, and shading are as in Figure 2. The combined variance in each band sums to $1-\lambda_{M=25}$. The colorbar and shading convention is as for Figure 2.

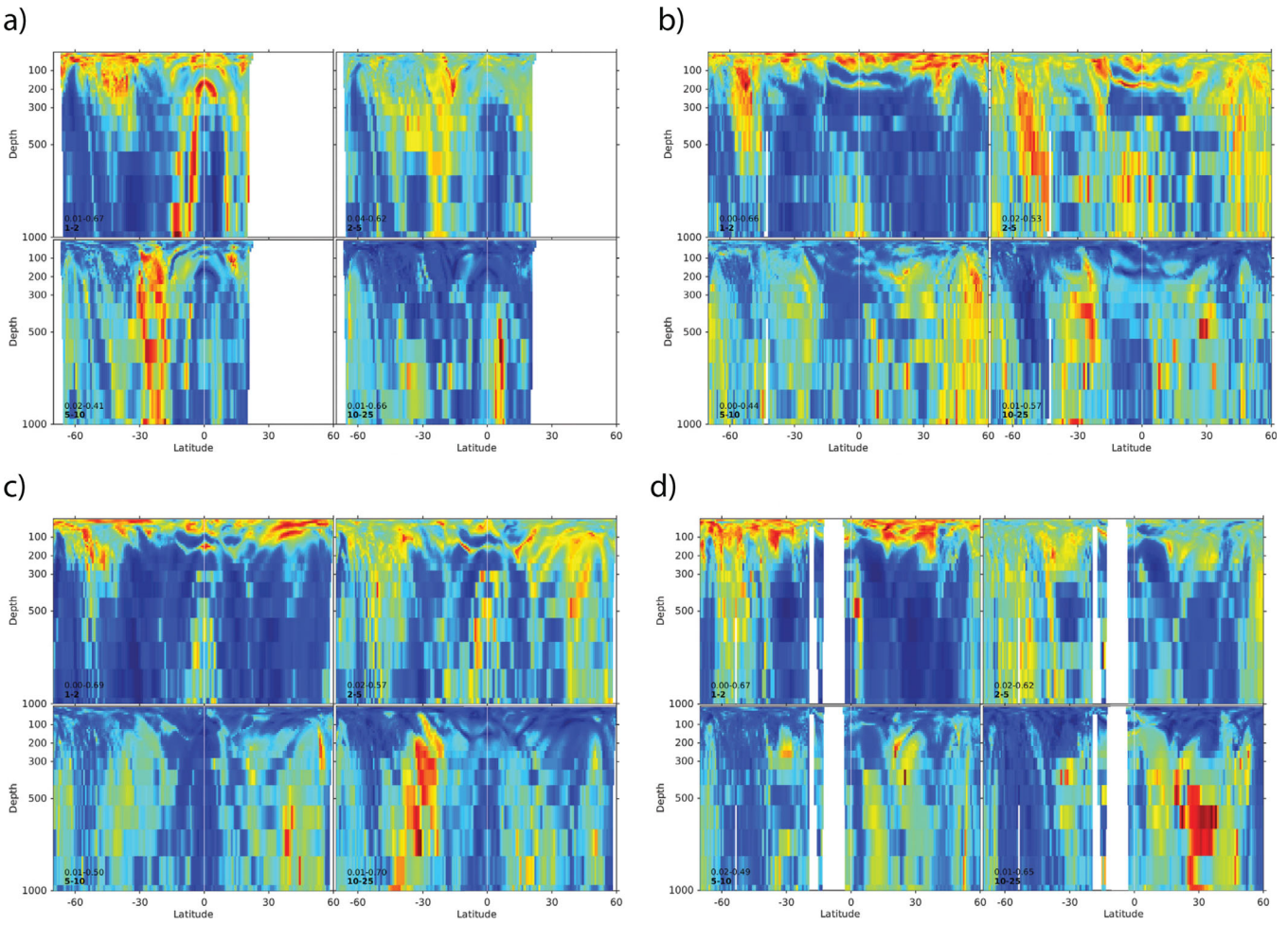

Figure 7. N^2 variances along latitudes 90°E, 180°E, 210°E, and 310°E calculated from the CORE2 forced coupled ocean-sea ice model. Again we use yearly anomalies from the climatological annual mean. Time scale bands, relative explained variance range, and shading are as in Figure 2. The combined variance in each band sums to $1-\lambda_{M=25}$. The colorbar and shading convention is as for Figure 2.

interested in the spatiotemporal patterns indicating regions of significant variability where unstable modes might occur.

In Figure 6, we show fractional in band variances of salinity for embeddings 1–2, 2–5, 5–10, 10–25 years and at depths of 105, 205, and 427m. For the 1–2 year time band, the signal is localized along the eastern tropical Pacific and the North Atlantic (all levels), the tropical Indian Ocean, and ACC particularly at 205 m depth. At 2–5 years, the most coherent signal at all levels are along the Western Australian-Indian Ocean. At 427 m, there is some variance along the eastern equatorial Pacific; however, further examination reveals this signal has little amplitude. At 5–10 years, the variance lacks coherence and is largely spread across the subtropical bands of both hemispheres at all levels. For 10–25 years, a very strong pattern of variability is evident along the South Pacific and in particular near 30°S, 180°E.

In Figure 7, we look at the vertical structure of the simulated fractional in band variances for the Brunt Väisälä frequency at longitudes of (a) 90°E, (b) 180°E, (c) 210°E, and (d) 320°E and to a depth of 1000 m. For the Indian Ocean along 90°E, the variability at 1–2 years is large along the equator about the thermocline $\approx$ 200 m with some surprising signal extending to depth at 20°S. Elsewhere, the variance is mostly contained within the ACC. At 2–5 years, the variance is again about the thermocline but between 15°S and 30°S. The 5–10 year band is mostly dominated by the signal of the Western Australian-Indian Ocean "storm track" along 30°S. Beyond 10 years, the signal is located to the North of the equator at $\approx$ 5° N about 500 m depth.

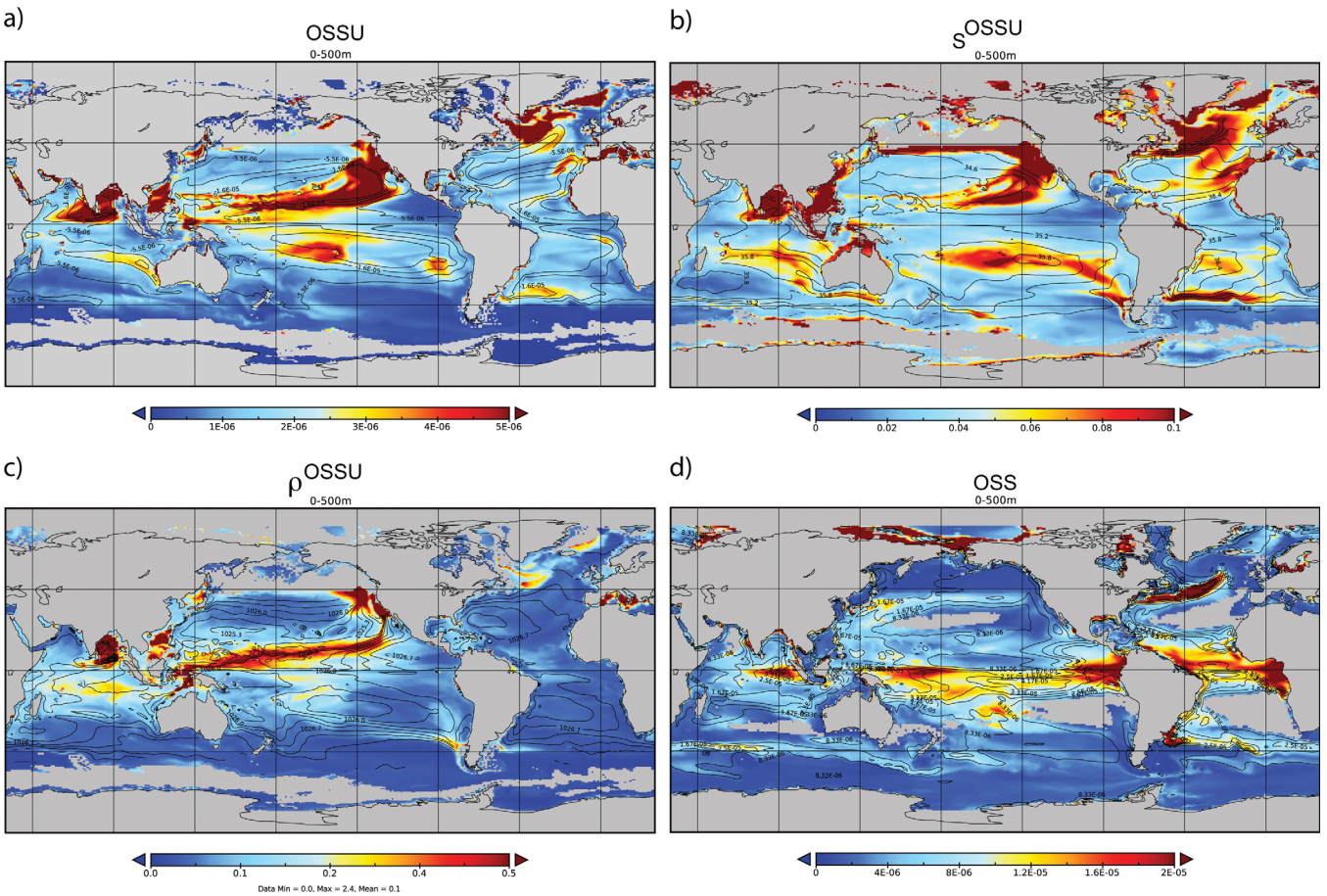

Figure 8. Average values (contours) and RMS variances (shaded) averaged over the upper 500 m of (a) $OSSU(s^{-2})$, (b) salinity $S(psu)$ where $OSSU$, (c) potential density $\rho(kg/m^3)$ where $OSSU$, and (d) $OSS(s^{-2})$ calculated from the CORE2 simulation. Grey regions occur where values are not present in the vertical average.

The variance in the Atlantic along 320°E is largely contained in the 1–2 year and the 10–25 year bands. In the former, the variance is largely in the upper 200 m to the South of the ACC. In the latter, it is localized about 500 m depth at 30°N in the region of the Sargasso Sea.

5.5. Ocean Salinity Stratification (OSS)

A calculation of *OSSU* and *OSS* from the 60 year CORE2 simulation is shown in Figures 8a and 8d, respectively. Here, the shading indicates the RMS variances calculated from monthly mean anomalies about the climatological average. We cannot apply SSA to the *OSSU* and *OSS* as either one may not exist in the water column at a given location and time and so we show anomalous RMS. The contours indicate the mean values taken over the entire period 1948–2007. Outside of the tropics, the largest signal occurs where the Gulf Stream separates from the East coast of North America, along the ACC at 45°S in the Indian and Atlantic Oceans.

In the South (North) Pacific oceans, the mean *OSSU* i.e., $\overline{OSSU}$ (Figure 8a), extends from the central (western) tropics to the South (North) American coast at about 20°S–30°S. In the North Indian Ocean, $\overline{OSSU}$ and $OSSU_{RMS}$ are largest in the Bay of Bengal extending into the equatorial region. For the SIO, *OSSU* occurs in a localized band extending from the Western Australian coast toward Madagascar. In the North Atlantic, significant $OSSU_{RMS}$ occurs in the region of the Greenland and Barents Seas. In the South Atlantic, $OSSU_{RMS}$ is mostly restricted to a region close to the Brazil-Malvinas Confluence.

Figure 8b shows salinity (S) where *OSSU* occurs averaged over the upper 500 m, i.e., S^{OSSU}. For salinity, the variance S^{OSSU}_{RMS} largely maps onto regions where the mean values of $\bar{S}^{OSSU}$ are largest with the structure of the S^{OSSU} mainly associated with the subtropical areas of high-salinity values (i.e., near the central positions of the main ocean gyres) and with the gradients on the poleward flanks. In the South Pacific, only S^{OSSU}_{RMS} is enhanced along the region from the coast of South America to the central Pacific. This indicates that once

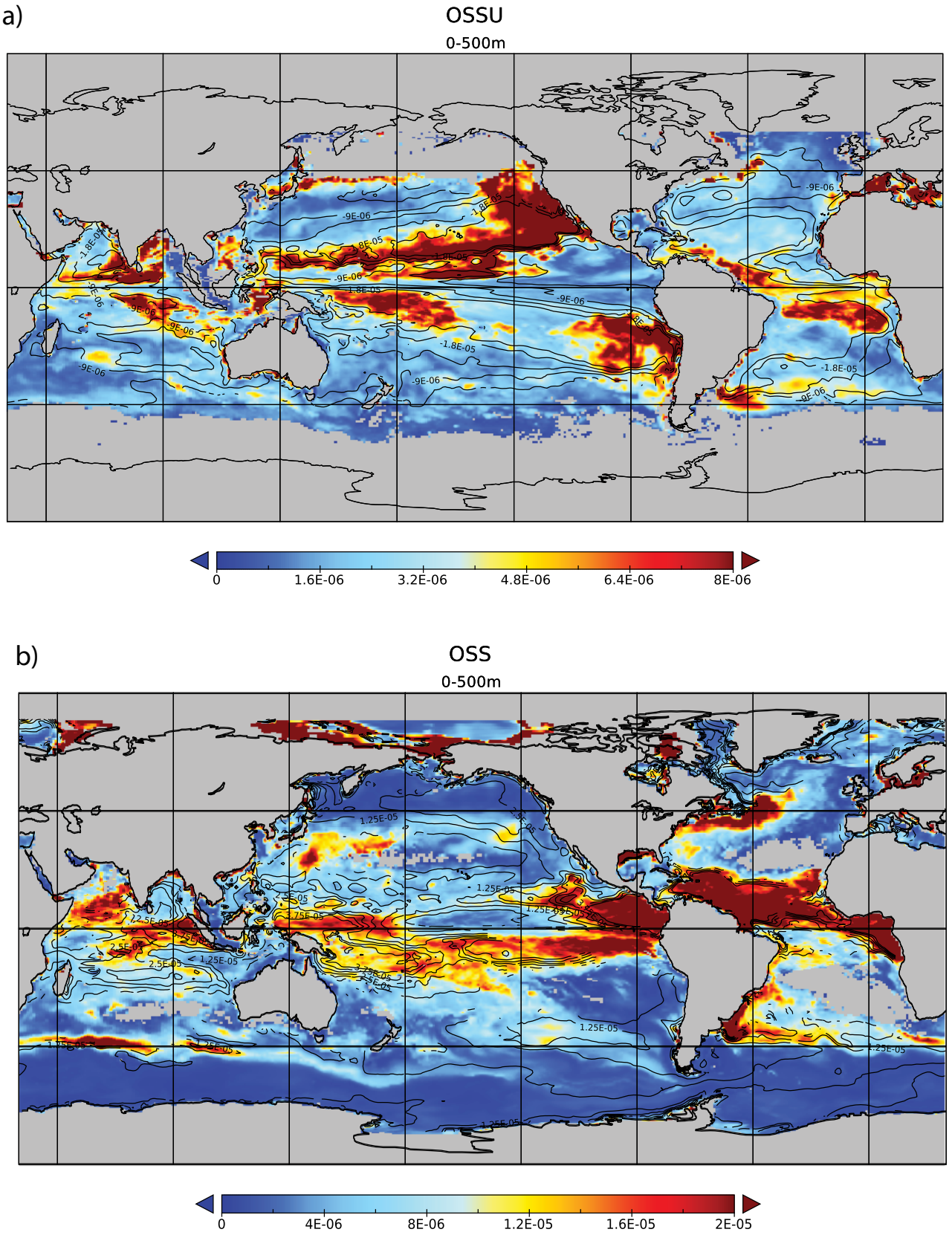

Figure 9. Average values (contours) and RMS variances (shaded) averaged over the upper 500 m of (a) $OSSU(s^{-2})$, (b) and $OSS(s^{-2})$ from the CSIRO reanalysis over the period January 2001 to December 2007. Grey regions occur where values are not present in the vertical average.

formed, warm and salty or cold and fresh anomalies remain largely coherent and are simply advected by the gyre circulation until impacting the equatorial Pacific thermocline, where they break up and generate $OSSU_{RMS}$ in the process. As expected, the other regions of large S^{OSSU}_{RMS} occur mostly coincident with $OSSU_{RMS}$. We further note that S^{OSSU}_{RMS} is largely coincident with *SSSA* in the 5–10 year band, as calculated from the CMIP5 model ensemble fractional in band variances (Figure 3). This would be consistent with the findings of *Lukas* [2001] showed that salinity variations in the upper thermocline are not simply correlated with temperature variations but are also strongly influenced by rainfall.

In Figure 8c, we show potential density averaged over the upper 500 m where *OSSU* occurs and denoted ρ^{OSSU}. While displaying largely similar spatial distributions in the mean, regions of ρ^{OSSU}_{RMS} and $OSSU_{RMS}$ display distinct hemispheric differences. More specifically, large values of ρ^{OSSU}_{RMS} occur in the Pacific along the Northern branch of the ITCZ and in the Bay of Bengal.

In order to establish some confidence in the spatial patterns of mean and anomaly RMS for *OSS* and *OSSU*, we show similar calculations using the CSIRO reanalysis over the period 2001–2007 after assimilating Argo, XBT, CTD, and satellite SST observations (Figure 9). This is a period for which there are sufficient observations to constrain the model upper ocean and where the reanalysis has been extensively analyzed and validated in previous studies [*O'Kane et al.*, 2014; *Maes et al.*, 2014; *Sloyan and O'Kane*, 2015] and in particular for the seasonal cycle of *OSS* [*Maes and O'Kane*, 2014]. Despite the restricted period, there is very good correspondence between the reanalyzed *OSS* and *OSSU* and the 60 year CORE2 model integration in both the mean and anomaly RMS for all fields (including S^{OSSU} and ρ^{OSSU} which are not shown). As is expected, the impact of assimilating observations is that the reanalyzed *OSS* and *OSSU* display more structure than the simulated *OSS* and *OSSU* in Figure 8; however, the broad-scale features are largely unchanged.

6. Summary of Results

Here we summarize the key results:

1. Intrinsic SSS variability is largely confined to the tropical Pacific (1–2 years) and the South Indian and North Atlantic subtropics (2–5 years).
2. On time scales of 1–2 years, internal SSS variability occurs largely in the tropical Pacific and Indian oceans with a close correspondence to the pattern of OSS_{RMS} where salinity acts to stabilize the stratification. At the 2–5 year time band, internal SSS variances move off the equator with the largest signal occurring in the region of the SPCZ and the Eastern part of the Indian Ocean. At 5–10 years, internal SSS variances move to the subtropical regions and are particular well correlated with the *OSSU*. This indicates an important role for the hydrological cycle on the variability of the upper ocean thermocline in the subtropics.
3. For the 10–25 year time band, we see a residual of the 5–10 year pattern, however the major signal in internal variability moves to the Southern Ocean sea-ice zone and specifically south of Cape Town.
4. For time band 25–50 years, coherent SSS variances occur in the South Pacific east of New Zealand and in the high latitudes of both hemispheres. Beyond 50 years, SSS variance is very small or negligible.
5. Salinity is shown to have a largely stabilizing effect on the upper ocean stratification in the upper 500 m of the tropical oceans. This is not the case for the subtropical Pacific ocean where salinity largely acts to destabilize and is closely associated with regions of density compensation. In particular, we posit that subtropical Pacific ocean $OSSU_{RMS}$ is a good indicator of the regions where spiciness anomalies form and decay. We show a clear pathway for the advection of such anomalies from the South East Pacific to the central equatorial Pacific. In the Northern Hemisphere such anomalies are systematically destroyed in the North Pacific by the influence of the northern branch of the ITCZ.
6. *OSSU* in the Bay of Bengal, SIO, and Atlantic ocean is found to be present in regions where coherent large-scale baroclinically unstable waves occur and are not associated with significant density compensation.

7. Discussion

7.1. Intrinsic SSS Variability

The intrinsic SSS variability observed in the 1–2 year time band (Figure 2) occurs predominantly in the tropical Pacific coincident with intrinsic sea surface height and SST variability previously described by *O'Kane*

et al. [2014]. They showed intrinsic variability in the central Pacific is representative of wave interferences which have a maximum in January–February. For CORE1 forcing, the equatorial Pacific region sees the same large-scale forcing each year, but responds in a highly nonlinear fashion to the small-scale random perturbations added to the winds with clear oscillations in the strength and spatial extent of these seasonal to interannual interferences.

O'Kane et al. [2014] developed a general theoretical framework describing nonlinear baroclinic disturbances and higher-order baroclinic-mode Rossby wave-mean flow interactions in the SIO. *Vargas-Hernandez et al*. [2015] provided observational evidence in support of that framework, describing westward moving and decadally varying salinity anomalies within the thermocline (depth of the 20°C isotherm) in the tropical SIO whose propagation speeds (between 0.4 and 1.7 cm/s) are slower than those of first baroclinic-mode Rossby waves or mean advection speeds of the background flow in the same regions. The anomalously slow propagation speeds described by *Vargas-Hernandez et al*. [2015] are consistent with the 2–5 year fractional in band variances seen in Figure 2 and with the EOF/PCA analysis of intrinsic SIO temperature anomalies described by *O'Kane et al*. [2014]. The intrinsic salinity variability reported here in combination with the studies referenced suggests a significant role for intrinsic ocean variability in determining large-scale coherent features in the SIO.

Gill et al. [1974], and later *Halliwell et al*. [1994], studied the partition of energy in the Sargasso Sea subtropical frontal zone. They showed that, initiated by the action of the mean wind field, the production of mid-ocean eddies occurs via conversion of the potential energy of the mean flow into transient energy and highlighted the primary role of nonlinearity once the wave number spectrum has saturated. *O'Kane et al*. [2014] showed that nonlinearity results in large-scale modification (meridional stretching) of baroclinically unstable waves occurring within waveguides associated with mean horizontal potential density gradients, particularly in the subtropical regions of the Southern Hemisphere (SH) oceans where the trade winds and westerlies meet, and at depths associated with mode water formation. *Hochet et al*. [2015] show recently that these are the regions where the largest fraction of the most unstable mode vertical structure is contained in the second baroclinic mode. The intrinsic SSS variability in the 2–5 year time band observed in the Sargasso Sea and extending into the Gulf Stream is generated by coherent large-scale salinity disturbances in the upper ocean, here shown in the animation of salinity anomalies at 200 m depth (supporting information). These disturbances occur in the large potential density gradients (both observed and modeled) described by *O'Kane et al*. [2014] (their Figure 4) and are of the same spatial-temporal scales as the baroclinic disturbances described by *Gill et al*. [1974].

Intrinsic variability in the 5–10 and 10–25 year time bands coincides with regions of large amplitude sea surface height and temperature variability in the South Pacific sector of the ACC previously examined in the study of *O'Kane et al*. [2013a, 2013b, 2013c]. They identified a Southern Ocean southeast Pacific intrinsic mode of low-frequency variability and further elucidated the excitation and amplification responses of this intrinsic mode to low-frequency atmospheric forcing (ENSO, Southern Annular Mode (SAM)) and stochastic forcing due to high-frequency winds. They showed how subsurface anomalies teleconnect the Pacific and Atlantic regions of the Antarctic Circumpolar Current (ACC) thermocline and that the Pacific region of the ACC can be characterized by intrinsic baroclinic disturbances that respond largely to the interannual winds associated with SAM and ENSO, while the Atlantic sector of the ACC is sensitive to synoptic winds that act to amplify thermocline anomalies propagating downstream from the Pacific.

7.2. Internal SSS Variability

The simulated 1–2 year internal fractional in band variances (Figure 3) in the tropics have spatial patterns broadly consistent with ENSO in the East Pacific, the Intercontinental Tropical Convergence Zone (ITCZ), and to some extent the Indian Ocean Dipole (IOD). This is somewhat different than a similar calculation of SLA and SSTA 1–2 year variances described by *Monselesan et al*. [2015] which were found to be predominantly due to ENSO alone. Spatial SSS patterns of fractional in band variances for the 1–2 and 2–5 year time bands are consistent with independent estimates of evaporation minus precipitation such as in Figure 5 of *Durack and Wijffels* [2010].

The observed shift of variance to the subtropics at 5–10 years and, in particular, in the South Eastern Pacific coincides with regions where large-scale warm and salty density compensated anomalies are known to be formed [*Kolodziejczyk and Gaillard*, 2012, 2013]. The potential for similar anomalies occurring in the North

Eastern Pacific [*Yeager and Large*, 2004, 2007] to impact the central Pacific thermocline and modulate ENSO have been the subject of intense investigation [*Luo and Yamagata*, 2001; *Luo et al*., 2005; *Schneider*, 2005; *O'Kane et al*., 2014]. *Lukas* [2001] showed the importance of the hydrological cycle as an active component of decadal climate variability in the North Pacific via density compensation of decadal thermal anomalies by salinity anomalies and that the T-S relationship in the North Pacific subtropical gyre varies nonlinearly in relationship to rainfall variability.

The SSS *SNR* (Figure 4) is consistent with results for SLA and SST in the recent study of *Monselesan et al*. [2015]. That $SNR > 1$ is an indication that the models, in large part, mostly agree on the regions where coherent low-frequency anomalous SSS variability occurs on multidecadal timescales (see fractional in band variances for each individual model in the supporting information). Here, *SNR* represents an estimate of confidence. In all time bands, the *SNR* is greater than 1—this degree of confidence is only achievable by considering many models and many thousands of years of data to robustly determine signal in the presence of noise. The high *SNR* i.e., > 6 in the 1–5 year time bands indicates a very high level of confidence in the resolved spatial patterns of interannual variability (i.e., red regions for both variance and SNR). Conversely, for the 100–200 year and longer time bands the *SNR* indicates a high degree of confidence that there is little or no variance (spread) in regions where $SNR > 6$ (i.e., blue regions for variance and red regions for *SNR*).We note that for any given time series we have only considered time bands less than the Nyquist-Shannon sampling frequency to avoid aliasing. Further, we have maximized the signal by normalizing the variances for each ensemble member prior to calculating the fractional in-band variances and then finally averaging these variances. This normalization step is required in order to aggregate the various model simulations.

7.3. Reanalyzed Versus Modeled Anomaly SSS

The lack of correspondence between the ORAS4 and CORE2 SSS anomaly variances compared to the CMIP5 simulations is an indication of the noisiness of SSS and the long integrations required to separate signal from noise. Returning to Figure 1, we see little correspondence between models and reanalyses prior to the early 1990s. ORAS4 in particular exhibits huge variations, such as between 1975 and 1985, that are not represented in the other products, apart from SODA which also has significant large variations. In contrast, GECCO2 displays little variability over the period prior to 1985. The forced ocean models DRAKKAR and CORE2 display largely similar variability over the early period prior to 1980. Over the latter period, post 1990 greater consensus emerges. In particular, the ORAS4, CSIRO and NCEP reanalyses are in reasonable agreement with GECCO2 consistently less variable. SODA is an extreme outlier during 1988–1992 and between 1998 and 2005. The forced ocean models are in reasonable agreement post 1990 largely tracking the ORAS4, CSIRO, and NCEP reanalyses to the mid to late 2000s. The lack of consensus across reanalyses (and forced models) in the tropics evident in Figure 1 and, in the ORAS4 and CORE2, 1–2 year fractional in band variances (Figure 5) is unsurprising, particularly given the inadequate data sampling at the global scale prior to Argo, differences in treating E-P forcing and the poor knowledge of the role of the adjustment of this freshwater flux.

The coherent subsurface salinity variance signals observed in the 2–5 years time band along the Western Australian-Indian Ocean sector between 20°S and 30°S are coincident with regions of high sea surface height anomalies observed in altimetry. *O'Kane et al*. [2014] examined this subtropical South Pacific Ocean pathway or "storm track." They identified the relevant structures as baroclinically unstable Rossby waves comparing their propagation characteristics to planetary Rossby waves calculated using a shallow water model. They show that such coherent propagating features are inherently nonlinear, multiscale, and are amplified where topography occurs. The location of the disturbances coincides with regions of high variability seen in Figure 6 and in sea surface height observed in satellite altimetry. They further showed that their propagation speeds closely match the large-scale coherent westward propagating structures described in the observational literature [*Maharaj et al*., 2009].

7.4. Static Stability

The Brunt Väisälä frequency variances (Figures 6 and 7) for the 1–2 year band in the Pacific along 180°E and 210°E occur largely in the upper 500 m in regions associated with the permanent thermocline (roughly between 30°S and 30°N). In the midlatitudes, the signal occurs about the seasonal thermocline including variability due to the low-frequency variations of the winter pycnocline. Again, variability associated with

the ACC is clearly evident between 45°S and 65°S along both longitudes down to about 500 m. In the 2–5 year band along 180°E, ACC variability is significant and extending down to 1000 m with a maximum at about 800 m. The structure of the equatorial Pacific thermocline is seen in the region corresponding to the western warm pool. The variance at about 40°S corresponds to the Kuroshio extension. The same patterns are largely manifest along 210°E but at somewhat reduced amplitudes. For the 5–10 year band, the variance is most coherent in the Northern Hemisphere at 180°E, 50°S. In the 10–25 year band, the signal along both 180°E and 210°E resides largely at 30°S within the South Pacific storm track.

7.5. Ocean Salinity Stratification

The regions of high variance in $\overline{OSSU}$ observed in Figure 8a in the subtropics in both hemispheres are coincident with regions where large-scale coherent density compensated anomalies are known to form [*Kolodziejczyk and Gaillard*, 2012, 2013; *O'Kane et al*., 2014]. Importantly, the *OSSU* anomaly RMS, denoted $OSSU_{RMS}$, in the North Pacific is broadly coincident with the high precipitation region of the Northern branch of the ITCZ before extending poleward to the western coast of North America. In the South East Pacific, $OSSU_{RMS}$ is largely coincident with regions associated with the formation of either warm and salty or cold and fresh anomalies, dependent on the strength of the wintertime isopycnal outcropping [*Kolodziejczyk and Gaillard*, 2012, 2013; *O'Kane et al*., 2014]. In the central Pacific near (190°E, 15°S), $OSSU_{RMS}$ is plausibly associated with the interaction of the density compensated anomalies with the permanent thermocline as described in *O'Kane et al*. [2014].

In the SIO, large variance in *OSSU* observed in a localized band extending from the Western Australian coast toward Madagascar (Figure 8b; also Figures 6 and 7a) occurs in regions associated with strong baroclinic instability, i.e., statically unstable, consistent with the studies of *O'Kane et al*. [2014] and *Vargas-Hernandez et al*. [2015]. Thus it is to be expected that salinity in these regions is contributing to anomalous destabilization of the water column.

In the North Pacific (Figure 8c), ρ^{OSSU}_{RMS} acts as a barrier to coherent spiciness anomalies. Specifically, the large anomalous density variations act to destroy any coherent spiciness anomalies from impacting the equatorial thermocline from the North. This is consistent with the findings of *Luo and Yamagata* [2001], who examined expendable bathythermograph (XBT) data showing that pronounced subsurface temperature anomalies propagating from the North Pacific are impeded due to the blocking effect of a potential vorticity barrier related to the Inter-Tropical Convergence Zone (ITCZ). The use of XBT observations assumes climatological salinity and hence any examination of the propagation of spiciness anomalies based on XBT data are not reliable. However, the results of Figure 8 add further weight to the idea that the ITCZ establishes a barrier impeding modulation of the equatorial Pacific thermocline by large-scale density compensated anomalies. The absence of any such barrier in the South Pacific, and recent robust observational examinations of South Pacific spiciness [*Kolodziejczyk and Gaillard*, 2012, 2013], are all consistent with the model results in Figure 8, showing no impediment to unstable coherent salinity anomalies impacting the equatorial Pacific thermocline.

Figure 8d reveals that both the mean *OSS*, denoted $\overline{OSS}$, and *OSS* anomaly RMS, denoted OSS_{RMS}, are both typically associated with the salinity barrier layer in the tropical Pacific regions of the Western Warm pool, the Eastern Pacific, to the west of Java, and in the tropical Atlantic, consistent with the study of *Maes and O'Kane* [2014].

Finally, one might question the realism of a model simply forced at the surface boundary by reanalyzed surface fluxes. To establish some confidence in the spatial patterns of mean and anomaly RMS, we repeat the calculations of *OSS* and *OSSU* using the CSIRO reanalysis over the period 2001–2007 finding very good correspondence between the reanalyzed *OSS* and *OSSU* and the 60 year CORE2 model integration. This result gives some confidence that the model integrations correctly simulate the broad patterns of upper ocean salinity variability.

8. Conclusions

We have shown that on timescales longer than the seasonal cycle, the significant uncertainties present in the large-scale spatial variations of SSS cannot be resolved with the present observational data sets. Moreover, observational records prior to Argo are insufficient to constrain current ocean general circulation models. Given this situation, we have estimated both intrinsic and internal modes of SSS variance using many

thousands of years of ocean and climate model data, thereby identifying regions of significant coherent SSS variability, either intrinsic to the ocean or in response to the interannually varying atmosphere. We next examined the spatiotemporal variability of upper ocean salinity across a hierarchy of forced ocean models and reanalyses, again partitioning the variance into time bands via application of singular spectral analysis and considering the Brunt Väisälä frequency (N^2) and the ocean salinity stratification in terms of the stabilizing effect due to the haline part of N^2 over the upper 500 m. For salinity variability in the upper 500 m, we find robust signals corresponding to the stabilizing role of salinity in the tropics, typically associated with heavy precipitation and barrier layer formation, and a destabilizing role in the subtropics in regions of low precipitation.

Our study points to the importance of salinity, not only at the surface and for the hydrological cycle, but in determining the variability and predictability of large-scale dynamical subsurface modes of variability of the main thermocline for timescales out to a few decades. The work presented here builds on recent modeling and reanalysis studies which will necessarily need to be revisited continually as critical observations and better performing models become available.

Appendix A: Model Configuration

The model is the Australian Community Climate Earth System Simulator-Ocean (ACCESS-O) configuration of the GFDL MOM4p1 ocean-ice code [*Delworth et al*., 2006]. A volume conserving approach based on the Boussinesq z^* coordinates scaled with depth along the vertical is used. The horizontal resolution is nominally 1° with equatorial refinement to $1/3^\circ$ in the tropical band between 10°S and 10°N and a Mercator (cosine dependent) implementation for the Southern Hemisphere applied, ranging from $1/4^\circ$ at 78°S to 10° at 30°S. In the vertical, ACCESS-O implements the z^* coordinate available in MOM4p1, with 50 model levels covering 0–6000 m with a resolution ranging from 10 m in the upper layers (0–200 m) to about 333 m for the abyssal ocean. Weak restoring is applied to the surface salinity of the top layer (equivalent thickness of 10 m) which is relaxed to world ocean atlas (WOA09) fields with a time scale of 60 days to reduce drift. The models horizontal resolution, while not eddy resolving, is still sufficient to capture the real ocean variability. An earlier study by *O'Kane et al*. [2013a, 2013b, 2013c] showed that, even without explicit eddies, this model has sufficient resolution to resolve Southern Ocean Rossby waves and energy transfers associated with transient disturbances interacting with the mean flow. Because of the prohibitive computational cost of eddy resolving models and the need for $>$1000 year spin-up runs to achieve steady state, the model resolution described represents a practical compromise and enables the study of decadal to climate timescale ocean dynamics.

Appendix B: CORE Experiments

The experiments described in this study employ atmospheric fields from the COREs [*Griffies et al*., 2009] for global ocean-ice modeling. For our experimental configuration, we use the CORE.v1 nominal year forcing and the CORE.v2 interannually varying forcing (1948–2007) [*Large and Yeager*, 2009], hereafter CORE1 and CORE2, respectively. Both CORE1 and CORE2 are supported at NCAR and GFDL for use in studying global ocean—ice dynamics and the CORE data sets, support code, and documentation were accessed from the GFDL MOM4 Data Sets website http://data1.gfdl.noaa.gov/nomads/forms/core/COREv2.html.

The spin-up uses CORE1 forcing with daily climatological atmospheric fields that are converted to air-sea fluxes with bulk formulas. The initial condition for temperature and salinity fields come from World Ocean Atlas 09 (WOA09), and the model was run with CORE1 forcing until a quasi-steady state with negligible drift was achieved after $\approx$ 1500 years. The spun up ocean state is used as an initial condition for all experiments reported herein. This CORE1 comprises a nominal year (1997) atmospheric forcing where the synoptic features are degraded by the addition of isotropic noise at the small scales. This configuration has been used to study intrinsic ocean modes of salinity variability and density compensation in the subtropics and tropics [*O'Kane et al*., 2014] and intrinsic baroclinic disturbances in the Southern Ocean [*O'Kane et al*., 2013a, 2013b, 2013c]. The CORE2 atmospheric forcing is time evolving and so contains synoptic, monthly, interannual, and longer-time scales.

Appendix C: CSIRO Reanalysis

The reanalysis is largely run with the model configuration described, with the additional constraint that the ocean temperature and salinity at depths below 2000 m are relaxed to WOA09 climatology with a 1 year

relaxation timescale as a proxy for lack of deep ocean observations. The model spin-up for the reanalysis consists of a further 60 year control integration (starting from year 1800 of the CORE1 spin-up) using CORE2 forcing with atmospheric fields that are converted to air-sea fluxes with bulk formulas [*Maes and O'Kane*, 2014]. Evaporation minus precipitation (E-P) fluxes are similarly adjusted consistently relative to the CORE2 forcing. Climatological river runoffs were employed in all simulations.

Model and observational data are synthesized using a variant of the BODAS ensemble optimal interpolation (EnOI) data assimilation system [*Oke et al*., 2008] to produce an ocean reanalysis for the period 1990–2007. The EnOI method employs background error covariances defined from a stationary, or time invariant, ensemble of anomalies (432 monthly mean anomalies w.r.t. the monthly climatological value) derived from the last 36 years of the control model integration.

Prior to January 1998, in situ profiles of temperature and salinity are assimilated from hydrographic data from World Ocean Circulation Experiment (WOCE) Hydrographic Program (WHP), World Ocean Database 2005 (WOD05; *Boyer et al*. [2006]), and the Quality controlled Ocean Temperature Archive (QuOTA; *Gronell and Wijffels* [2008]), which contains all XBT data in the Indian and southwest Pacific Oceans. After January 1998, we assimilate the WOCE Upper Ocean Thermal (UOT) database that includes global XBT data, except in the Indian Ocean where we use QuOTA for XBTs. Temperature and salinity are assimilated from Argo profiles and from the TAO array [*Oke et al*., 2013].

A series of global reanalyses were performed as part of an Observing System Experiment (OSE) to quantify the successive impact, relative to the control model (CTRL), of subsurface temperature and salinity profiles (R_T/S), satellite SST (R_$^+$ SST) and altimetric data (R_ALL). Here we show only results for the R_$^+$ SST variant. Background error covariances are localized according to the Shur product method of *Gaspari and Cohn* [1999]. As both our model and observational spatial resolution is of the order of 1°, we employ a localization length scale of 8°. Analysis updates are introduced gradually into the model integration to ensure consistency with the background innovations and to reduce model shock [*Bloom et al*., 1996]. A major advantage of EnOI is that the background error covariances are inhomogeneous and anisotropic and therefore better reflect the variability and length scales of the ocean circulation [*Oke et al*., 2008]. At each update step, the adaptive initialization scheme of *Sandery et al*. [2011] is employed, ensuring more balanced initial conditions than is possible using Newtonian relaxation. The updated variables are temperature, salinity, and surface height. We employ a 15 day centerd observational window for the R_$^+$ SST reanalysis such that the observational window is dependent on the quantity of data available, computational constraints, model resolution, and a desire not to have overlapping windows. The update cycle for the reanalysis matches the observational window. SST observations are identified within a given grid cell after which we compute the super observation position as the average position of all observations. These observations are then combined, using a simple weighted average, yielding the super observation following the method of [*Oke et al*., 2008]. The errors of all observations are used to compute an appropriate error for the superobservation using standard error propagation techniques. More detailed discussions of the assimilation method, OSE, and error statistics are reported elsewhere [*Maes and O'Kane*, 2014; *Sloyan and O'Kane*, 2015].

Acknowledgments

T. J. O. was funded by an Australian Research Council Future Fellowship (grant FT120100008). C.M. is supported by IRD and CNES under the TOSCA program dedicated to the ESA-SMOS satellite mission. D.P.M. is supported by the Australian Climate Change Science Program. CSIRO reanalyses and ocean model data were generated by and are managed by T.J.O. We acknowledge the World Climate Research Programme's Working Group on Coupled Modeling, which is responsible for CMIP, and we thank the climate modeling groups (listed in Table 1 and the supporting information of this paper) for producing and making available their model output. For CMIP, the U.S. Department of Energy's Program for Climate Model Diagnosis and Intercomparison provides coordinating support and led development of software infrastructure in partnership with the Global Organization for Earth System Science Portals.

References

Allen, M., R. M. Dettinger, M. D. Ide, K. Kondrashov, D. Mann, M. E. Robertson, A. Saunders, Y. Tian, F. Varadi, and P. Yiou (2002), Advanced spectral methods for climatic time series, *Rev. Geophys.*, *40*(1), 1003, doi:10.1029/2000RG000092.

Antonov, J. I., S. Levitus, and T. P. Boyer (2002), Steric sea level variations during 1957–1994: Importance of salinity, *J. Geophys. Res.*, *107*(C12), 8013, doi:10.1029/2001JC000964.

Balmaseda, M. A., K. Mogensen, and A. T. Weaver (2013), Evaluation of the ECMWF ocean reanalysis system ORAS4, *Q. J. R. Meteorol. Soc.*, *139*, 1132–1161.

Bloom, S. C., L. L. Takacs, A. M. da Silva, and D. Ledvina (1996), Data assimilation using incremental analysis updates, *Mon. Weather Rev.*, *124*, 1256–1271.

Boyer, T. P., S. Levitus, J. Antonov, R. Locarnini, and H. Garcia, (2005), Linear trends in salinity for the World Ocean, 1955–1998. *Geophys. Res. Lett.*, *32*, L01604, doi:10.1029/2004GL021791.

Boyer, T. P., J. I. Antonov, H. Garcia, D. R. Johnson, R. A. Locarnini, A. V. Mishonov, M. T. Pitcher, O. K. Baranova, and I. Smolyar (2006),*World Ocean Database 2005*, chap. 1, *NOAA Atlas NESDIS 60*, edited by S. Levitus, 182 pp., U.S. Gov. Print. Off., Washington, D. C.

Cravatte, S., T. Delcoix, D. Zhang, M. McPhaden, and J. LeLoup, (2009), Observed freshening and warming of the western Pacific warm pool, *Clim. Dyn.*, *33*, 565–589.

Curry, R., B. Dickson, and I. Yashayaev (2003), A change in the freshwater balance of the Atlantic Ocean over the past four decades, *Nature*, *426*, 826–829.

Delcroix, T., S. Cravatte, and M. J. McPhaden, (2007), Decadal variations and trends in tropical Pacific sea surface salinity since 1970, *J. Geophys. Res.*, *112*, C03012, doi:10.1029/2006JC003801.

Delworth, T., A. Broccoli, A. Rosati, R. Stouffer, V. Balaji, J. Beesley, W. Cooke, and K. Dixon (2006), GFDL, CM2 global coupled climate models. Part 1: Formulation and simulation characteristics, *J. Clim. 19*, 643–674.
Durack, P. J., and S. E. Wijffels (2010), Fifty-year trends in global ocean salinities and their relationship to broad-scale warming, *J. Clim.*, *23*, 4342–4362.
Durack, P. J., S. E. Wijffels, and R. J. Matear (2012), Ocean salinities reveal strong global water cycle intensification during 1950 to 2000, *Science*, *336*, 455–458.
Elsner, J. B., and A. A. Tsonis (1996), *Singular Spectrum Analysis, A New Tool in Time Series Analysis*, Plenum Press, N. Y.
Font, J., et al. (2013), SMOS first data analysis for sea surface salinity determination, *Int. J. Remote Sens.*, 1–7, doi:10.1080/01431161.2012.716541.
Gaspari, G., and S. Cohn (1999), Construction of correlation functions in two and three dimensions, *Q. J. R. Meteorol. Soc.*, *125*, 723–757.
Gill, A., J. Green, and A. Simmons (1974), Energy partition in the large-scale ocean circulation and the production of mid-ocean eddies, *Deep Sea Res. Oceanogr. Abstr.*, *21*, 499–528.
Golyandina, N., and A. Zhigljavsky (2013), *Singular Spectrum Analysis for Time Series, Springer Briefs in Statistics*, Springer, U. K.
Griffies, S., et al. (2009), Coordinated Ocean-ice reference experiments (CORE)s, *Ocean Modell.*, *26*, 1–46.
Grodsky, S. A., J. A. Carton, and F. M. Bingham (2006), Low frequency variation of sea surface salinity in the tropical Atlantic, *Geophys. Res. Lett.*, *33*, L14604, doi:10.1029/2006GL026426.
Gronell, A., and S. E. Wijffels (2008), A semiautomated approach for quality controlling large historical ocean temperature archives, *J. Atmos. Oceanic Technol.*, *25*, 990–1003.
Halliwell, G., G. Peng, and D. Olson (1994), Stability of the Sargasso sea subtropical frontal zone, *J. Phys. Oceanogr.*, *24*, 1166–1183.
Hochet, A., T. Huck, and A. Colin de Verdière (2015), Large-scale Baroclinic instability of the mean oceanic circulation: A local approach, *J. Phys. Oceanogr.*, *45*, 2738–2754.
Hosoda, S., T. Sugo, N. Shikama, and K. Mizuno (2009), Global surface layer salinity change detected by Argo and its implication for hydrological cycle intensification, *J. Oceanogr.*, *65*, 579–586.
Kerr, Y., P. Waldteufel, J. P. Wigneron, S. Delwart, F. Cabot, J. Boutin, M. J. Escorihuela, J. Font, N. Reul, and C. Gruhier (2010), The SMOS mission: New tool for monitoring key elements of the global water cycle. *Proc. IEEE*, *98*(5), 666–687.
Kolodziejczyk, N., and F. Gaillard (2012), Observation of spiciness interannual variability in the Pacific pycnocline, *J. Geophys. Res. 117*, C12018, doi:10.1029/2012JC008365.
Kolodziejczyk, N., and F. Gaillard (2013), Variability of the heat and salt budget in the subtropical southeastern Pacific mixed layer between 2004 and 2010: Spice injection mechanism, *J. Phys. Oceanogr.*, *43*, 1880–1898.
Large, W., and S. Yeager (2009), The global climatology of an interannually varying air sea flux data set, *Clim. Dyn.*, *33*, 341–364.
Lagerloef, G. S. E. (2012), Satellite mission monitors Ocean surface Salinity, *Eos Trans. AGU*, *93*(25), 233–234, doi:10.1029/2012EO250001.
Lagerloef, G. S. E., et al. (2008), The Aquarius/SAC-D mission: Designed to meet the salinity remote sensing challenge, *Oceanography*, *21*(1), 68–81.
Luo, J.-J., and T. Yamagata (2001), Long-term El Niño-Southern Oscillation (ENSO)-like variation with special emphasis on the South Pacific, *J. Geophys. Res. 106*, 22,211–22,227.
Luo, Y., L. M. Rothstein, R. -H. Zhang and A. J. Busalacchi (2005), On the connection between South Pacific subtropical spiciness anomalies and decadal equatorial variability in an ocean general circulation model, *J. Geophys. Res. 110*, C10002, doi:10.1029/2004JC002655.
Lukas, R. (2001), Freshening of the upper thermocline in the North Pacific subtropical gyre associated with decadal changes of rainfall, *Geophys. Res. Lett. 28*, 3485–3488.
Maes, C. (2008), On the ocean salinity stratification observed at the eastern edge of the equatorial Pacific warm pool, *J. Geophys. Res.*, *113*, C03027, doi:10.1029/2007JC004297.
Maes, C., and T. J. O'Kane (2014), Seasonal variations of the upper ocean salinity stratification in the Tropics, *J. Geophys. Res. Oceans*, *119*, 1706–1722, doi:10.1002/2013JC009366.
Maes, C., N. Reul, D. Behringer, and T. J. O'Kane (2014), The salinity signature of the equatorial Pacific cold tongue as revealed by the satellite SMOS mission, *Geosci. Lett.*, *1*, 1–7. [Available at http://www.geoscienceletters.com/content/1/1/17.]
Maharaj, A., P. Cipollini, and N. Holbrook (2009), Multiple westward propgating signals in South Pacific sea level anomalies, *J. Geophys. Res.*, *114*, C12016, doi:10.1029/2008JC004799.
Matear, R. J., T. J. O'Kane, J. S. Risbey, and M. A. Chamberlain (2015), Sources of heterogeneous variability and trends in Antarctic sea-ice, *Nat. Commun.*, doi:10.1038/ncomms9656.
Monselesan, D. P., T. J. O'Kane, J. S. Risbey, and J. Church (2015), Internal climate memory in observations and models, *Geophys. Res. Lett.*, *42*, 1232–1242, doi:10.1002/2014GL062765.
O'Kane, T. J., R. J. Matear, M. A. Chamberlain and P. R. Oke (2013a), ENSO regimes and the late 1970s climate shift: The role of synoptic weather and South Pacific ocean spiciness, *J. Comput. Phys.*, *271*(2014), 19–38.
O'Kane, T. J., R. J. Matear, M. A. Chamberlain, J. S. Risbey, B. M. Sloyan, and I. Horenko (2013b), Decadal variability in an OGCM Southern Ocean: Intrinsic modes, forced modes and metastable states, *Ocean Modell.*, *69*, 1–21.
O'Kane, T. J., J. S. Risbey, C. L. E. Franzke, I. Horenko, and D. P. Monselesan (2013c), Changes in the meta-stability of the mid-latitude Southern Hemisphere circulation and the utility of non-stationary cluster analysis and split flow blocking indices as diagnostic tools, *J. Atmos. Sci. 70*(3), 824–842.
O'Kane T. J., R. J. Matear, M. A. Chamberlain, E. C. J. Oliver, and N. J. Holbrook (2014), Storm tracks in the Southern Hemisphere subtropical oceans, *J. Geophys. Res. Oceans*, *119*, 6078–6100, doi:10.1002/2014JC009990.
Oke, P. R., G. Brassington, D. Griffin, and A. Schiller (2008), The Bluelink Ocean Data Assimilation System (BODAS), *Ocean Modell.*, *21*, 46–70.
Oke, P. R., et al. (2013), Towards a dynamically balanced eddy-resolving ocean reanalysis: BRAN3, *Ocean Modell.*, *67*, 52–70, doi:10.1016/j.ocemod.2013.03.008.
Reul, et al. (2014), Sea surface salinity observations from space with the SMOS satellite: A new means to monitor the marine branch of the water cycle, *Surv. Geophys.*, *35*, 681–722, doi:10.1007/s10712-013-9244-0.
Roemmich, D., and J. Gilson (2009), The 2004–2008 mean and annual cycle of temperature, salinity, and steric height in the global ocean from the Argo Program, *Prog. Oceanogr.*, *82*, 81–100.
Sandery, P. A., G. B. Brassington, and J. Freeman (2011), Adaptive nonlinear dynamical initialization, *J. Geophys. Res.*, *116*, C01021, doi:10.1029/2010JC006260.
Schneider, N. (2005), The response of tropical climate to the equatorial emergence of spiciness anomalies, *J. Clim. 17*, 1083–1095.
Sen Gupta, A., L. C. Muir, J. N. Brown, S. J. Phipps, P. J. Durack, D. P. Monselesan, and S. E. Wijffels (2012), Climate drift in the CMIP3 models, *J. Clim.*, *25*, 4621–4640.

Sen Gupta, A., N. C. Bourdain, J. N. Brown, and D. P. Monselesan (2013), Climate drift in the CMIP5 models, *J. Clim.*, *26*, 8597–8615.
Sloyan, B. M., and T. J. O'Kane (2015), Drivers of decadal variability in the Tasman Sea, *J. Geophys. Res. Oceans*, *120*, 3193–3210, doi:10.1002/2014JC010550.
Taylor, K., R. Stouffer, and G. Meehl (2012), An overview of CMIP5 and the experiment design, *Bull. Am. Meteorol. Soc.*, *93*(4), 485–498.
Yu, L. (2012), A global relationship between the ocean water cycle and near surface salinity, *J. Geophys. Res.*, *116*, C10025, doi:10.1029/2010JC006937.
Vargas-Hernandez, M., S. E. Wijffels, G. Meyers, and N. J. Holbrook (2015), Slow westward movement of salinity anomalies across the tropical South Indian Ocean, *J. Geophys. Res. Oceans*, *120*, 5436–5456, doi:10.1002/2015JC010933.
Yeager, S., and W. Large (2004), Late-winter generation of spiciness on subducted isopycnals, *J. Phys. Oceanogr. 34*, 1528–1547.
Yeager, S. and W. Large (2007), Observational evidence of winter spice injection, *J. Phys. Oceanogr. 37*, 2895–2919.